Advances in Computational Design, *Vol. 9, No. 3 (2024) 167-186*
https://doi.org/10.12989/acd.2024.9.3.167

Isogeometric micromechanical damage analysis of fiber-reinforced composites by presenting a single-patch framework

Ali Hosseinzadeh[a], Mohammad Reza Forouzan* and Mehdi Karevan[b]

Department of Mechanical Engineering, Isfahan University of Technology, Isfahan, 84156-83111, Iran

(Received March 10, 2023, Revised July 31, 2024, Accepted September 11, 2024)

Abstract. Implementing isogeometric methodology in micromechanical analysis of composite materials has been recently investigated in some research studies. These research studies are based on multi-patch modeling which requires coupling constraints among the NURBS patches, and the domain decomposition effort in model preparation stage. This approach has been employed for small representative volume elements (RVE). However, small RVE neglects some characteristics of microstructure and larger one increases the number of required NURBS patches in multi-patch framework. As a step forward, this research presents a framework which simulates the RVE using a single NURBS patch. the presented framework has been used to include the effects of fiber distribution and porosities in simulated RVEs. In this regard, heterogeneity and 2D/3D voids within RVE are modeled only by inserting knots and modifying the control points. In addition to beneficial advantages of isogeometric methodology for RVE-based models, this framework simplifies isogeometric modeling of more complicated RVEs by eliminating the domain decomposition stage and avoiding coupling constraints between non-matching patches. The performance of the presented model has been verified by performing micromechanical damage analysis on several generated RVEs of unidirectional fiber-reinforced composites, in which matrix and fiber/matrix interfaces experience damage. The predicted damage evolutions under different loading conditions are in excellent agreement with prior experimental and numerical studies that demonstrate the veracity of the presented model.

Keywords: damage analysis; fiber-reinforced composites; isogeometric analysis; micromechanics; porosity

1. Introduction

Currently, many vital parts are produced with lightweight composite materials. The durability and mechanical performance of these parts are strongly dependent on microstructure and manufacturing defects. Physical experiments and computational micromechanics are two practical approaches to studying the microstructural characteristics and defects of composite materials. Experimental tests provide realistic results of microstructural events. On the other hand, in computational micromechanics, various environmental and loading states that experimentally are difficult to test can be numerically simulated on a representative volume element (RVE) of the microstructure. In this approach, the finite element method (FEM) is employed as the main

*Corresponding author, Professor, E-mail: forouzan@cc.iut.ac.ir
[a] Ph.D. Student, Email: ali.hosseinzadeh@me.iut.ac.ir
[b] Assistant Professor, Email: mkarevan@iut.ac.ir

 ISSN: 2383-8477 (Print), 2466-0523 (Online)

computational tool for micromechanical simulations. Computational micromechanics is widely used to evaluate failure modes (Melro *et al*. 2013) and estimate the macroscopic properties (Terada *et al*. 2000) of composite materials.

In micromechanical models, it's hence essential to choose an appropriate RVE with adequate geometrical details to obtain realistic responses. Specifically, for unidirectional fiber-reinforced composites (UD-FRC), fiber size and distribution, volume fraction, defects of voids, separation of fiber/matrix interface, and other micro-scale characteristics should be considered in RVE as similar as possible to the real material. In this regard, experimental observations on the microstructure of UD-FRC have revealed that fibers are mainly dispersed in the matrix in a random distribution (González and LLorca 2007, Naya *et al*. 2017). Therefore, a large RVE with numerous fibers is required to consider the effects of fiber distribution. For these RVEs, to strike a balance between obtaining realistic results and minimizing the computational costs, adequate RVE size has been investigated (Arefi *et al*. 2020). However, the adequate size reported in the literature may increase by changing the characteristics of RVE. For example, to investigate the effects of high aspect-ratio inter-fiber and in-matrix micro-voids (~2 μm), Ashouri *et al*. (2015) employed an RVE containing 70 fibers with ~48000 linear triangular elements. On the other hand, for the larger cylindrical voids (~60 μm), Mehdikhani *et al*. (2019b) generated a huge RVE containing ~2000 fibers with ~470,000 hexahedral elements.

For micromechanical modeling of UD-FRC with large RVE size and containing many fibers, conventional FEM simulation suffers from some shortcomings such as requiring vast numbers of elements and degrees of freedom, long times, and significant computational expenses. Also, large RVEs need long mesh generation and model preparation process to build the analysis model from the geometrical representation (Dokken *et al*. 2009). However, this process should be totally regenerated by any change in RVE. Specifically, this gap is the major contributor to time consumption in sequential simulations in which some details (e.g., a fiber, a void, or a primary crack) are changing within RVE. Furthermore, in FEM, geometry is approximated by Lagrangian polynomial shape functions, which are less accurate in complex geometries.

Over the last decade, isogeometric analysis (IGA) based on knot vectors and Non-Uniform Rational B-Spline (NURBS) basis functions has become a robust analytic methodology in engineering applications. Hughes *et al*. (2005), revealed that IGA could eliminate some restrictions of FEM by integrating both computer-aided design (CAD) and computer-aided engineering (CAE) representations without applying the mesh generation stage. Owing to the known advantages of IGA, this methodology has been widely implemented in various numerical engineering problems. Integrating the geometrical and analysis representations and the capability of exact drawing geometry with few degrees of freedom have made the IGA methodology interesting for shape and topology optimization problems (López *et al*. 2021). Also, the smoothness of NURBS basis functions makes this methodology suitable for structural analysis of plates and shells (Guo *et al*. 2019), contact mechanics (Dimitri and Zavarise 2017), inverse analysis (Shamloofard and Assempour 2019) and variety of other engineering applications (Willberg 2016). Moreover, IGA has been used in damage mechanics problems (Rawat *et al*. 2021, Verhoosel *et al*. 2011b). In this regard, damage analysis of composite materials has been studied on various shapes of plates (Deng *et al*. 2015), shells (Alaydin *et al*. 2022, Pigazzini *et al*. 2018), and other engineering parts (Bazilevs *et al*. 2015). However, the previous studies were on the macroscopic scale, whereas the heterogeneity and other micro-scale characteristics of the composites have been neglected. So far, the performance of IGA in the application to micro-scale damage analysis of composite materials has not been examined.

Nevertheless, IGA encounters some geometric complexities in a NURBS patch such as discontinuity, heterogeneity, and internal voids, which should be considered in microstructure modeling of composites. In some studies, discontinuity has been considered by adding enrichment functions to the NURBS basis function, which is known as the extended isogeometric analysis (XIGA) (Bhardwaj *et al*. 2021, De Luycker *et al*. 2011). On the other hand, Verhoosel *et al*. (2011a) and Nguyen *et al*. (2014) revealed that separation and cohesive zones can be modeled by inserting repetitive knots in IGA methodology. For instance, This technique has been used in delamination analysis of composite materials by Nguyen *et al*. (2014).

Over the past recent years, a few techniques have been presented to model heterogeneity and multiple internal voids in IGA Methodology. However, most of the previous studies have focused on voids with 2D shapes. In one approach, IGA has been combined with other methodologies. In this regard, Ruess *et al*. (2014) and Guo *et al*. (2017) presented a technique through the combination of IGA and Finite Cell Method for the analysis of plates and shells with internal cutouts. On the other hand, Bhardwaj *et al*. (2015) and Singh *et al*. (2015) used the concept of XIGA to model holes and inclusions in a domain by adding Heaviside and distance functions, to the NURBS basis functions. They used this methodology in fracture mechanics analysis of cracked heterogeneous materials (Bhardwaj *et al*. 2015, Bhardwaj and Singh 2015). Adding the concept of T-splines is another approach have been proposed to model internal holes in NURBS patches (Sederberg *et al*. 2008). Another approach, known as multi-patch IGA, is based on drawing several patches and connecting them by introducing coupling constraints (Chan *et al*. 2019, Guo *et al*. 2017). In this regard, Alberdi *et al*. (2018) presented a framework based on multi-patch approach (MPA) for RVE-based problems. For instance, a unit-cell containing circular inclusion was modeled by introducing nine patches. In addition, Matsubara *et al*. (2017) suggested the use of MPA to model heterogeneity and impose periodic boundary conditions for homogenization analysis. In this regard, they employed 16 patches for unit-cell of UD-FRC containing a single fiber. However, for RVEs of UD-FRC, number of required patches of MPA increases by raising the number of fibers and/or voids.

The primary purpose of this research is to introduce an isogeometric framework for micromechanical analysis of composite materials which is appropriate for different RVE sizes. In this regard, the RVE is modeled in a single-patch framework (SPF) to prevent the excessive increase of the required patches in larger and more complicated RVEs. In this framework, the microstructural details of composites including heterogeneity and porosity are modeled by some geometry modification techniques, based on the features of NURBS functions. These techniques are adequately simple to be used for any number of fibers and 2D/3D voids within RVE. Also, Adding the inclusions and voids does not require regenerating of the RVE discretization. Obviously, this advantage is very beneficial for design purposes that need sequential simulations. In terms of applications, the presented techniques have been used to study the effects of cylindrical and spherical micro-voids on mechanical responses. Eventually, the performance of the presented SPF-IGA has been examined in micromechanical damage analysis of randomly distributed UD-FRCs.

2. Background theory

The concepts of NURBS, and IGA method are presented in the following subsections briefly. Details can be found in (Hughes *et al*. 2005).

2.1 B-spline and NURBS

B-splines are piecewise polynomial functions that parametrically represent curves, surfaces, or volumes. B-spline is defined over a non-descending sequence in the parametric space $\Xi = \{\xi_1, \xi_2, \ldots, \xi_{n+p+1}\}$ known as a knot vector. ξ_i, p and n are the ith knot, the polynomial order, and the number of basis functions, respectively. B-spline basis functions with p order are recursively calculated using the Cox–de Boor formula (Hughes *et al*. 2005):

$$N_{i,0} = \begin{cases} 1 & \xi_i \le \xi < \xi_{i+1} \\ 0 & otherwise \end{cases} \tag{1}$$

$$N_{i,p}(\xi) = \frac{\xi - \xi_i}{\xi_{i+p} - \xi_i} N_{i,p-1}(\xi) + \frac{\xi_{i+p+1} - \xi}{\xi_{i+p+1} - \xi_{i+1}} N_{i+1,p-1}(\xi) \tag{2}$$

where ξ is the parametric variable. Among the advantages of the B-spline, the capability of making various orders of continuity by changing knots repetitions can be mentioned. In general form, the non-zero basis functions with the order of p haveC^{p-g} continuity on the $\xi = \xi_i$, where g is the number of repetitions of ξ_i in the knot vector.

Non-uniform rational B-spline (NURBS), the generalized form of B-spline, is generated by assigning weights (w_i) to the basis functions as follows:

$$R_{i,p}(\xi) = \frac{N_{i,p}(\xi) w_i}{\sum_{\hat{\imath}=1}^{n} N_{\hat{\imath},p}(\xi) w_{\hat{\imath}}} \tag{3}$$

By considering the set of basis functions and a control points net (C), NURBS curve, surface and volume are obtained by the following equations:

$$L(\xi) = \sum_{i=1}^{n} R_{i,p}(\xi) \quad C_i = \sum_{i=1}^{n} \frac{N_{i,p}(\xi) \;\; w_i \;\; C_i}{\sum_{\hat{\imath}=1}^{n} N_{\hat{\imath},p}(\xi) \;\; w_{\hat{\imath}}} \tag{4}$$

$$S(\xi, \eta) = \sum_{i=1}^{n} \sum_{j=1}^{m} \frac{N_{i,p}(\xi) M_{j,q}(\eta) w_{i,j} C_{i,j}}{\sum_{\hat{\imath}=1}^{n} \sum_{\hat{\jmath}=1}^{m} N_{\hat{\imath},p}(\xi) M_{\hat{\jmath},q}(\eta) w_{\hat{\imath},\hat{\jmath}}} \tag{5}$$

$$V(\xi, \eta, \zeta) = \sum_{i=1}^{n} \sum_{j=1}^{m} \sum_{k=1}^{t} \frac{N_{i,p}(\xi) M_{j,q}(\eta) T_{k,r}(\zeta) w_{i,j,k} C_{i,j,k}}{\sum_{\hat{\imath}=1}^{n} \sum_{\hat{\jmath}=1}^{m} \sum_{\hat{k}=1}^{t} N_{\hat{\imath},p}(\xi) M_{\hat{\jmath},q}(\eta) T_{\hat{k},r}(\zeta) w_{\hat{\imath},\hat{\jmath},\hat{k}}} \tag{6}$$

where $N_{i,p}(\xi)$, $M_{j,q}(\eta)$ and$T_{k,r}(\zeta)$ are single-variable B-spline basis functions and p, $q$and r are the polynomial order of basis functions related to Ξ, $H = \{\eta_1, \eta_2, \ldots, \eta_{m+q+1}\}$ and $Z = \{\zeta_1, \zeta_2, \ldots, \zeta_{t+r+1}\}$ knot vectors, respectively.

2.2 Isogeometric analysis (IGA)

In NURBS-based IGA, NURBS geometry is drawn by the definition of knot vectors, basis functions, weights, and control points net and simultaneously, field variables are approximated using the same NURBS basis functions. Therefore, spatial coordinates (X) and field variable (U)

are formulated as represented below:

$$X(\xi,\eta)=\sum_{i=1}^{n}\sum_{j=1}^{m}R_{i,j}(\xi,\eta)X_{i,j} \tag{7}$$

$$U(\xi,\eta)\approx\sum_{i=1}^{n}\sum_{j=1}^{m}R_{i,j}(\xi,\eta)U_{i,j} \tag{8}$$

where $X_{i,j}$ and $U_{i,j}$ are control points coordinates and control variables, respectively. In Eq. (7), physical geometry is converted to the uniform domain using a NURBS mapping known as parametric space. Moreover, IGA Elements are defined as non-zero knot spans $[\xi_i,\xi_{i+1}],\xi_i\neq\xi_{i+1}$ in the parametric space.

3. RVE's SPF build-up

In this section, some step-by-step techniques are presented to model the geometrical and constitutive details of UD-FRC, including heterogeneity, voids, and fiber/matrix debonding. Capabilities of the method have been used to model UD-FRC RVE, in the next sections.

3.1 RVE's Geometrical modeling in NURBS representation

Fig. 1 shows a unit-cell, including a square matrix and a circular fiber as a simple RVE. Initially, four paths $\xi=0,1;\ \ \eta=0,1$ are required to determine the unit-cell boundaries. Next, the fiber/matrix boundary can be obtained by drawing the suggested four paths $\xi=\xi_1,\xi_2;\ \ \eta=\eta_1,\eta_2$ $(0<\xi_1<\xi_2<1$ and $0<\eta_1<\eta_2<1)$, as displayed in Fig. 1(a). As shown in this figure, each path is covering a part of the fiber-matrix interface without any subscription region. In the next step, each path is assigned to a unique knot in the knot vector. Owing toC^0 continuity at intersection points, repetitive knots should be inserted in $\xi=\xi_1,\xi_2$ and $\eta=\eta_1,\eta_2$. Consequently, by considering second-order basis functions and equal spacing knots, the resultant knot vectors can be expressed as:

$$\Xi=H=\left\{0,0,0,\frac{1}{3},\frac{1}{3},\frac{2}{3},\frac{2}{3},1,1,1\right\} \tag{9}$$

According to uniform geometry along the fiber direction, a simple first-order knot vector can be considered for the third-knot vector as $Z=\{0,0,1,1\}$. In the next step, the corresponding parametric space and control points are defined based on knot vectors and specified paths. For the set of the mentioned knot vectors, parametric space is divided into 8 IGA elements of the matrix material and one IGA element of fiber which is visualized in Fig. 1(b).

Since the selected knot vectors for geometry are utilized for displacements approximation (field variables in this study), the order of continuity of displacements on the fiber-matrix interface is of great importance. If fiber and matrix are perfectly bonded,C^0continuity can be considered for displacement components. Thus, the aforementioned knot vectors are consistent for displacement approximations. However, if interfacial debonding takes place,C^{-1} continuity can be achieved by adding other repetitive knots at $\xi=\frac{1}{2},\frac{1}{3}$ and $\eta=\frac{1}{2},\frac{1}{3}$ as formerly reported by Verhoosel *et al*.

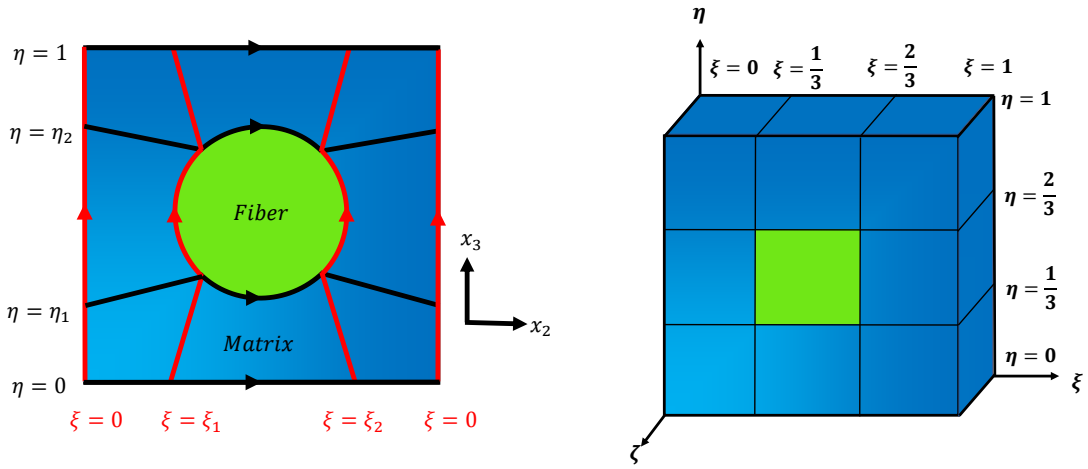

(a) suggested paths for the NURBS representation (b) parametric space

Fig. 1 Unit-cell build-up through the single-patch NURBS representation

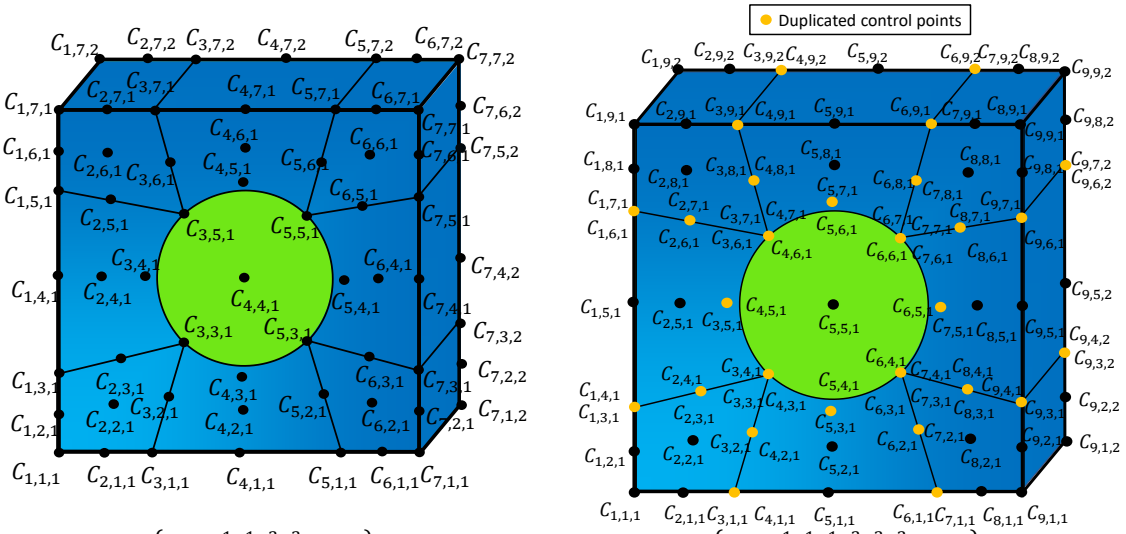

(a) $\Xi = H = \left\{0,0,0,\frac{1}{3},\frac{1}{3},\frac{2}{3},\frac{2}{3},1,1,1\right\}; Z = \{0,0,1,1\}$ (b) $\Xi = H = \left\{0,0,0,\frac{1}{3},\frac{1}{3},\frac{1}{3},\frac{2}{3},\frac{2}{3},\frac{2}{3},1,1,1\right\}; Z = \{0,0,1,1\}$

Fig. 2 Physical space with control points

(2011a) and Nguyen *et al*. (2014). The modified set of knot vectors is then changed to:

$$\Xi = H = \left\{0,0,0,\frac{1}{3},\frac{1}{3},\frac{1}{3},\frac{2}{3},\frac{2}{3},\frac{2}{3},1,1,1\right\};\quad Z = \{0,0,1,1\} \tag{10}$$

As shown in Fig. 2, making C^{-1}continuity leads to duplicating the control points along the corresponding path. Consequently, interfacial debonding can be simulated by the separation of duplicated points. However, in this technique, several duplicated points are located in the regions except the fiber-matrix interface. To avoid discontinuity in these regions, different choices can be made. For instance, the concept of T-splines (Bazilevs *et al*. 2010) can be employed to eliminate

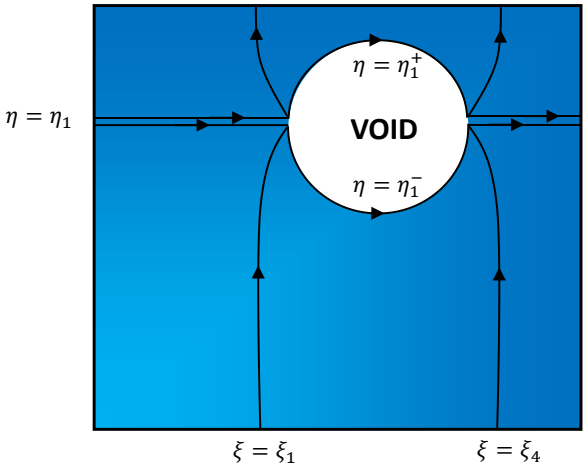

Fig. 3 Unit-cell with cylindrical void

the redundant control points. but in this study, simple tie constraints were applied to the duplicated control points. It must be noted that the location of tie constraints can be parametrically determined that helps the user to define the constraints automatically by employing a subroutine program.

Finally, nonrepetitive knot insertion and degree elevation can be applied to increase the accuracy of displacement approximation (Hughes *et al*. 2005). Although, this subsection presented for a unit-cell build-up, it can be generalized to more complicated RVEs with more reinforcing fibers by increasing the number of specified paths. It must be mentioned that each described path can pass through several fibers' boundaries.

3.2 Modeling of voids in RVE

Two types of voids are common in fiber-reinforced composites: spherical and cylindrical. The former serves as a low aspect ratio, while the latter is a high one. These typical geometries are not the only shapes of voids; others are such as ellipsoidal, needle, flattened, and irregular cross-section shapes (Mehdikhani *et al*. 2019a), which can be modeled in the same way. In these techniques, voids are generated within RVE only by inserting knots and relocating a few control points. Using this technique brings two advantages: (1) this technique does not employ any extra NURBS patch, and (2) it is not necessary to regenerate the RVE discretization.

3.2.1 Prismatic cylindrical voids

The results of several studies show that micron-sized voids may be elongated in the longitudinal direction with circular or elliptical cross-sections and high aspect ratio (~40) (Gurdal *et al*. 1991). Therefore, micro-voids can be simulated in a 2D framework, as shown in Fig. 3. In this way, voids are similar to fibers geometrically, but the specified void domain should not occupy the parametric space. According to Fig. 3, a cylindrical void can be modeled in RVE by identifying three paths. First, a C^{-1} continuous path $\eta = \eta_1$ is inserted with two intersection points on the boundary of void. Consequently, two rows of control points are duplicated, forming two paths including $\eta = \eta_1^-, \eta_1^+$. These two paths coincide on the regions out of void border, while the paths

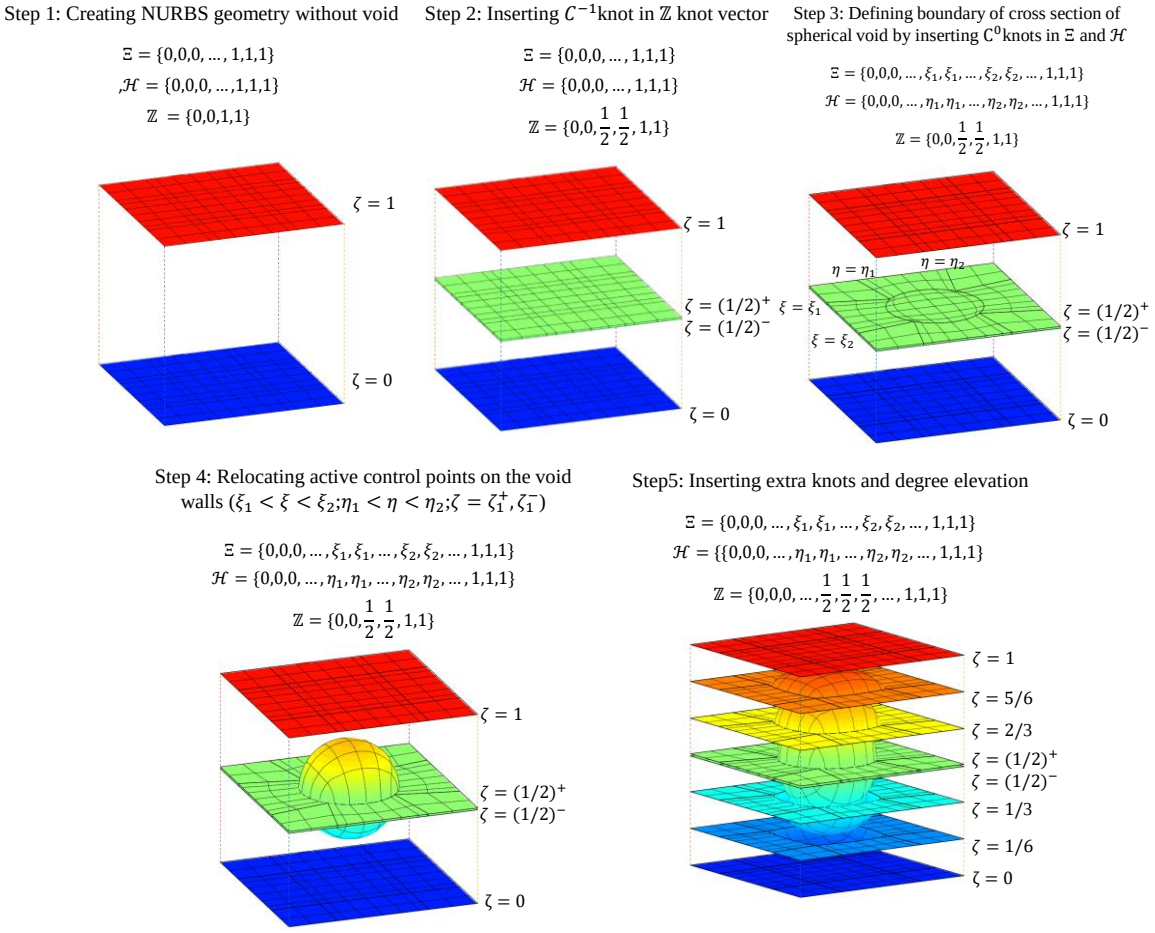

Fig. 4 Steps in creating spherical void in the NURBS geometry of RVE

between the intersection points are separate and each one passes half of void border. Thereafter, two repetitive knots $\xi = \xi_1, \xi_2$ will be inserted to model C^0 continuity at the intersection points. Due to the prismatic shape of Void, no change is needed on the Z knot vector.

3.2.2 Spherical voids

The step-by-step offered technique for modeling spherical voids is presented in Fig. 4. Modeling of spherical void is started by insertingC^{-1} continuous knot along the fiber direction as $Z = \left\{0,0,\frac{1}{2},\frac{1}{2},1,1\right\}$. Therefore, the NURBS geometry of RVE can be represented by four surfaces including $\zeta = 0, \frac{1^+}{2}, \frac{1^-}{2}, 1$. In the next step, the cross-section of void is defined in $\zeta = \frac{1^+}{2}, \frac{1^-}{2}$ surfaces by adding four C^0 continuous knots $\xi = \xi_1, \xi_2$ and $\eta = \eta_1, \eta_2$, as also discussed in Section 3.1. Afterward, the shape of spherical void is modeled by relocating the control points and fitting the separated surfaces on the void walls. This step is operated on the control points with nonzero basis functions within the domain $\xi_1 < \xi < \xi_2;\ \eta_1 < \eta < \eta_2;\ \zeta = \frac{1^+}{2}, \frac{1^-}{2}$.

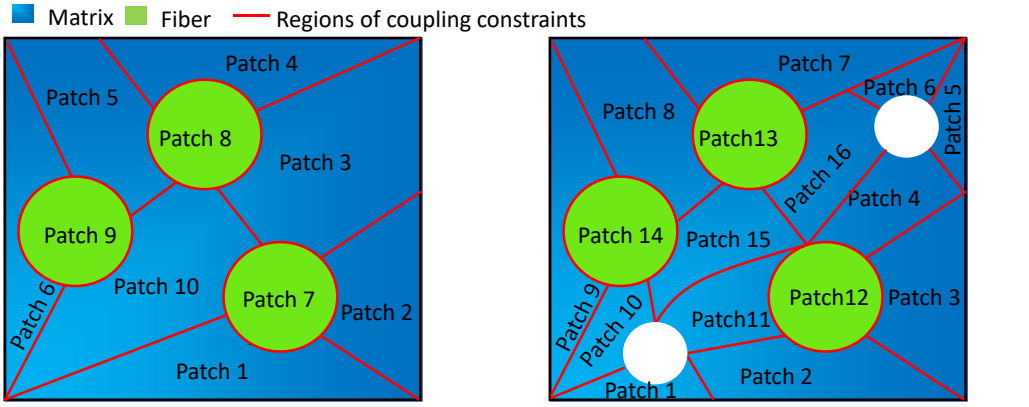

$\Xi^i = \{0,0,0,\xi_1^i,\xi_2^i,\xi_3^i,\xi_4^i,\dots,1,1,1\}$
$H^i = \{0,0,0,\eta_1^i,\eta_2^i,\eta_3^i,\eta_4^i,\dots,1,1,1\}$; $i = 1{:}10$

(a) RVE containing three fibers

$\Xi^i = \{0,0,0,\xi_1^i,\xi_2^i,\xi_3^i,\xi_4^i,\dots,1,1,1\}$
$H^i = \{0,0,0,\eta_1^i,\eta_2^i,\eta_3^i,\eta_4^i,\dots,1,1,1\}$; $i = 1{:}16$

(b) After adding two voids

Fig. 5 NURBS patches and required knot vectors in MPA

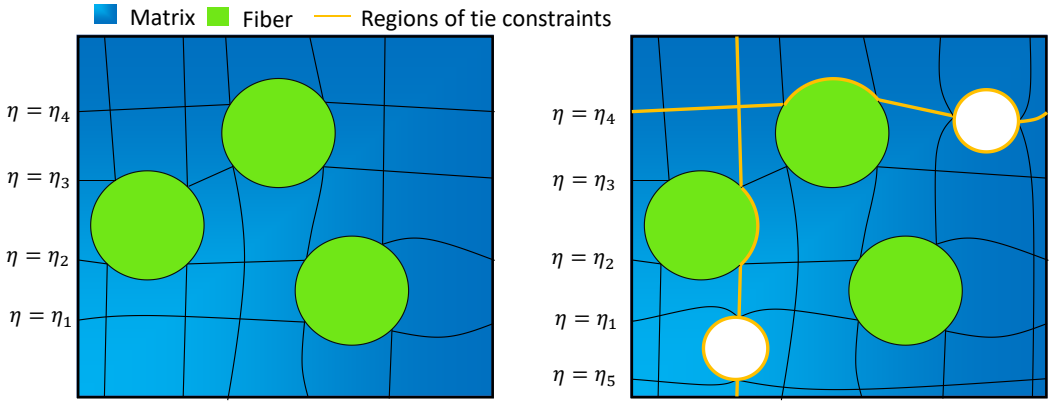

$\xi = \xi_1 \;\; \xi = \xi_2 \;\; \xi = \xi_3 \;\; \xi = \xi_4 \;\; \xi = \xi_5$

$\Xi = \{0,0,0,\xi_1,\xi_1,\xi_2,\xi_2,\xi_3,\xi_3,\xi_4,\xi_4,\xi_5,\xi_5,1,1,1\}$

$H = \{0,0,0,\eta_1,\eta_1,\eta_2,\eta_2,\eta_3,\eta_3,\eta_4,\eta_4,1,1,1\}$

(a) RVE containing three fibers

$\xi = \xi_1 \;\; \xi = \xi_2 \;\; \xi = \xi_3 \;\; \xi = \xi_4 \;\; \xi = \xi_5 \;\; \xi = \xi_6$

$\Xi = \{0,0,0,\xi_1,\xi_1,\xi_2,\xi_2,\xi_2,\xi_3,\xi_3,\xi_4,\xi_4,\xi_5,\xi_5,\xi_6,\xi_6,1,1,1\}$

$H = \{0,0,0,\eta_5,\eta_5,\eta_1,\eta_1,\eta_2,\eta_2,\eta_3,\eta_3,\eta_4,\eta_4,\eta_4,1,1,1\}$

(b) After adding two voids

Fig. 6 NURBS patch and required knot vectors in the presented SPF

3.3 Advantages of SPF build-up

To describe the advantages of the presented SPF-IGA for RVE-based micromechanical models, a comparison is made to MPA. Fig. 5(a) depicts an RVE including three circular fibers decomposed to 10 irregular NURBS patches in MPA. Thereafter, adjacent patches are connected by introducing coupling constraints in common borders. Since the used knot vectors and control points on coupled edges are not necessarily matched, the coupling constraints are often extracted from complex equations (Chan *et al*. 2019, Yildizdag *et al*. 2020). Furthermore, adding some details (two cylindrical voids in this example) change the patches and coupling constraints significantly (Fig. 5(b)).

Table 1 Comparison of MPA-IGA and presented SPF-IGA

Multi-patch approach	Presented single-patch framework
Geometry is built-up by numerous NUBS patches that requires a domain decomposition stage	Geometry is built-up by only a single NURBS patch
By adding new details to RVE, the NURBS patches and the coupling constraints must be regenerated	New Details can be considered by inserting knots and modifying few control points
coupling constraints are complicated	constraints are simple ties on duplicated points
Solution process deals with numerous knot vectors, nets of control points and variables	Solution process deals with one set of knot vectors, one control points net and one control variables net
Control points on opposite sides of the RVE are not similar, therefore, applying the periodic boundary conditions is difficult	Control points on opposite sides of the RVE are similar, which simplifies applying the periodic boundary conditions

In contrast, the RVE depicted in Fig. 6(a), has been generated in SPF by defining a few paths and assigning each path to a unique knot. Then, the addition of voids can be performed by minor modifications comprising adding few knots and modifying some control points (Fig. 6(b)). Also, despite the manually coupling constraints in MPA, automatically programmable tie constraints along C^{-1} paths do not increase the preparation time significantly. Other properties of the presented SPF-IGA and MPA-IGA can be found in Table 1.

4. IGA-based micromechanical damage analysis

To demonstrate the veracity of the presented IGA-based model, several RVEs were generated. Then, mechanical responses were investigated under different loading conditions. All used material properties for glass/epoxy are given in Table 2. Glass fibers were modeled isotropic and linear elastic. A pressure-dependent isotropic elastic-damage model, presented by Arefi *et al*. (2018), was employed for epoxy matrix with an exponential softening law for the stress-strain curve under uniaxial tension. In this model, Young's modulus (E_m) and Poisson's ratio (ν_m) are degraded simultaneously by the same damage parameter (d). Also, a parabolic damage criterion is used for damage initiation and propagation to consider pressure dependency behavior in constitutive equations:

$$F = \frac{3\tilde{J}_2}{X_t X_c} + \frac{\tilde{I}_1(X_c - X_t)}{X_t X_c} - r = 0 \tag{11}$$

where X_t and X_c are tensile and compressive strengths. $\tilde{I}_1$ and $\tilde{J}_2$ are the invariants of the effective stress tensor (Arefi *et al*. 2018). Also, r is damage progression variable that corresponds to the maximum loading during loading history.

Cohesive zone modeling formulation presented by Turon *et al*. (2006) was utilized for the fiber-matrix interface. According to this model, damage initiation occurs when the traction on the interface reaches to:

$$T^0 = \sqrt{{T_n^0}^2 + \frac{({T_s^0}^2 - {T_n^0}^2)\beta^{2\mu}}{(1 + 2\beta^2 - 2\beta)^{\mu}}} \tag{12}$$

Table 2 Material properties

E-glass fiber					
Young's modulus (E_f)			Poisson's ratio (v_f)		
74000 Mpa			0.2		
Epoxy matrix					
Young's modulus (E_m)	Poisson's ratio (v_m)	Tensile strength (X_t)	Compressive strength (X_c)	Mode I fracture toughness (G_m)	
3760 Mpa	0.39	93 Mpa	124 Mpa	0.09 N/mm	
Fiber/matrix interface (cohesive zone modeling)					
Initial stiffness (K_0)	Tensile strength (T_n)	Shear strength (T_s)	Mode I fracture energy (G_{IC})	Mode II fracture energy (G_{IIC})	BK law parameter (μ)
10^8 MPa/mm	50 Mpa	70 Mpa	2 J/m2	6 J/m2	1.45

where T_n^0 and T_s^0 are normal and shear interfacial strengths, μ is a constant material property and β is mode mixity parameter defined as:

$$\beta = \frac{\Delta_s}{\langle \Delta_n \rangle + \Delta_s} \tag{13}$$

where Δ_n and Δ_s are normal and shear components of separation between fiber and matrix. Also, damage evolution in a bilinear traction separation law is calculated by a single variable equivalent separation parameterλwhich is expressed as:

$$\lambda = \sqrt{\langle \Delta_n \rangle^2 + \Delta_s^2} \tag{14}$$

To apply the described cohesive interfacial behavior in SPF-IGA, IGA cohesive Elements were employed between the fiber and matrix elements. Eventually, applying IGA cohesive zone modeling in specified parametric regions gives traction-separation relations between duplicated control points (Nguyen *et al*. 2014).

Periodic boundary conditions (PBCs) were applied by employing constraints on each pair of control points on opposite external sides (Barbero 2008). Also, various loading conditions were performed by applying macroscopic strains ε_{ij}^0 at the corners (Melro *et al*. 2013). As the results, damage distribution, ultimate strength, and stress-strain curves were obtained using the following homogenized stress definition (Melro *et al*. 2013):

$$\bar{\sigma}_{ij} = \frac{1}{V}\int_V \sigma_{ij} dV \tag{15}$$

5. Results and discussion

The presented single-patch isogeometric framework was exerted to build up two RVEs for analyzing micromechanical damage in UD-FRC, with and without micro-voids. In the first case, a three-dimensional periodic RVE of Fig. 7(a) with a fiber volume fraction of ~%60 was considered by including 25 randomly distributed fibers with a diameter of d_f=5μm.

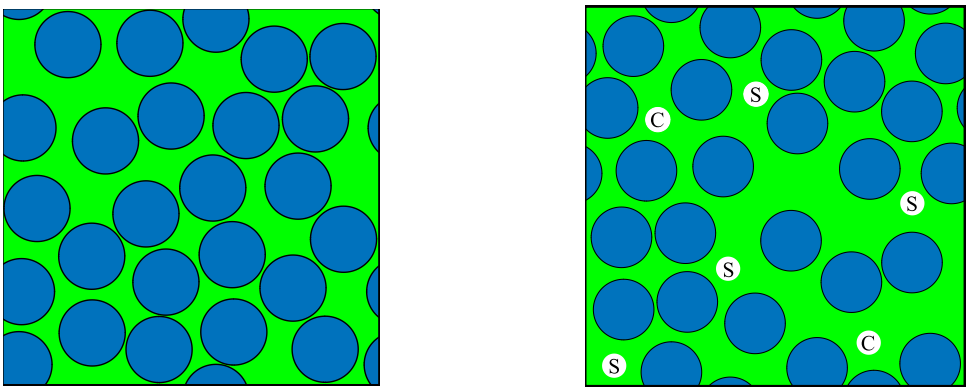

C: cylindrical micro-void S: spherical micro-void

(a) ~60% fiber volume fraction

(b) ~50% fiber volume fraction and ~1% mixed cylindrical/spherical micro-voids

Fig. 7 Generated RVEs

The second case focused on the modeling of porosity in IGA methodology. The RVE depicted in Fig. 7(b) was generated with a fiber volume fraction of ~50%; it contained small micro-voids with a diameter of $d_v = 0.4d_f$ (Ashouri Vajari *et al*. 2014) and a void volume fraction of ~1%. The mixed cylindrical/spherical micro-voids (with the volume fraction proportion of 0.7% and 0.3%, respectively) were randomly distributed in matrix. As a result, the effects of the presence of voids on mechanical responses were investigated.

The RVEs were created by second-order basis functions in transverse directions (Ξ and H). For the RVE displayed in Fig. 7(a), due to the uniformity of strain components along the fiber's axis, a linear knot vector with one layer of element $Z = \{0,0,1,1\}$ was selected. However, this was not the case for RVEs containing spherical micro-voids, and the selected knot vector for RVE of Fig. 7(b) is discussed in Section 5.2.

5.1 Example 1-Damage evaluation in UD-FRC, without micro-voids, under basic load cases

In this section, the mechanical responses of the generated RVE, as represented in Fig. 7(a), were studied in four basic loading conditions: Transverse tension, Transverse shear, Longitudinal shear, and Transverse compression. For a better evaluation of the presented model, micromechanical simulations were performed in two types of fiber/matrix interfacial behaviors, including perfect-bonding and cohesive zone modeling.

The presented SPF-IGA was verified by comparing its outputs and the results obtained by using conventional linear 8-node brick elements in FEM. As shown in Fig 8(a), a comparison of the extracted transverse tension strength from FEM solutions and IGA with ~4000 elements showed that IGA accurately obtained the results and considerably decreased the required degrees of freedom. Also, a small difference between the ~4000 and ~6800 elements of IGA solutions revealed that the selected IGA discretization provided adequate accuracy for converging solutions. This agreement was observed similarly for longitudinal shear loading in Fig. 8(b) and demonstrated that the selected IGA discretization could be appropriate for other types of loading conditions.

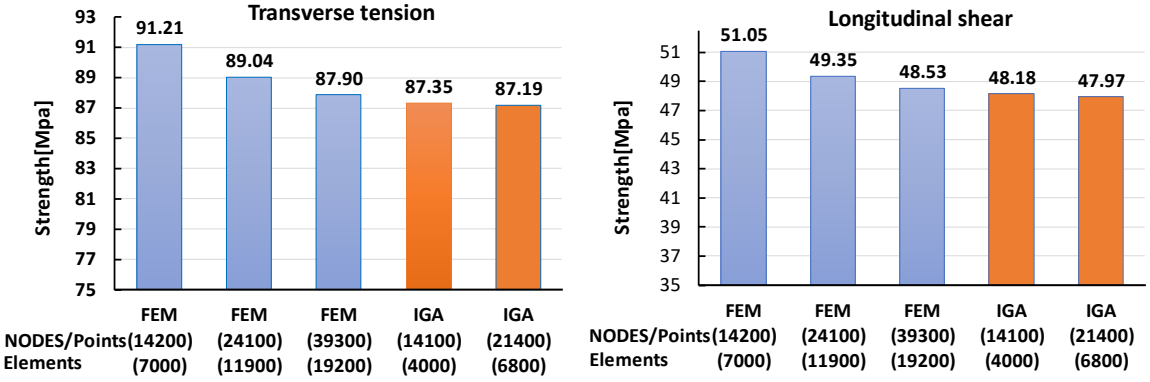

(a) Transverse tension (b) Longitudinal shear

Fig. 8 Comparison of IGA and FEM solutions for different number of elements and degrees of freedom

Table 3 Obtained strengths for different loading cases

fiber/matrix interfacial behavior	Strength [Mpa]			
	Transverse tension	Transverse compression	Transverse shear	Longitudinal shear
Perfect-bonding	87.4	133.9	52.8	48.2
Cohesive zone modeling	49.3	132.1	44.2	48.4

Comparison of averaged strength results, as represented in Table. 3, with and without cohesive elements showed a significant difference under transverse tension loading, which could be attributed to different failure mechanisms between them. By assuming fiber/matrix perfect-bonding, microcracks were initiated in two different regions: (1) near the fiber/matrix interfaces of closely fibers and (2) in the middle of the distance between fibers which were more spaced. The described failure events can be observed in Fig. 9(a), which is in agreement with the presented results by Arefi *et al*. (2018).

On the other hand, by employing cohesive elements, fibers were separated from matrix due to the weakness of normal interfacial strength. Then, the carried load was transferred to the matrix (Fig. 10(a)). Eventually, the final crack was developed perpendicular to loading direction, which was completely compatible with the experimental observations of Canal *et al*. (2012).

Field Damage distribution for transverse compression loading can be found in Figs. 9(b) and 10(b). In both figures, microcracks were developed in a direction with 53° angle perpendicular to the loading direction, which was similar to other numerical (Naya *et al*. 2017) and experimental (Puck and Schürmann 2002) studies. Also, damage distribution in Fig.9(c) shows that microcracks initiation near fiber/matrix interfaces is the main reason for failure under longitudinal shear. In this type of loading, no interfacial debonding could be observed throughout RVE. Therefore, no meaningful difference could be seen with and without cohesive elements.

Under transverse shear loading without cohesive elements, the observed failure mechanisms were similar to longitudinal shear loading, and the final crack was developed in a horizontal plane (Fig. 9(d)). However, Fig. 10(c) demonstrates that in the presence of interfacial cohesive behavior, failure mechanisms are completely different and failure takes place due to two different sequences of events. First, several fiber/matrix interfaces are deboned throughout RVE. Afterward, the

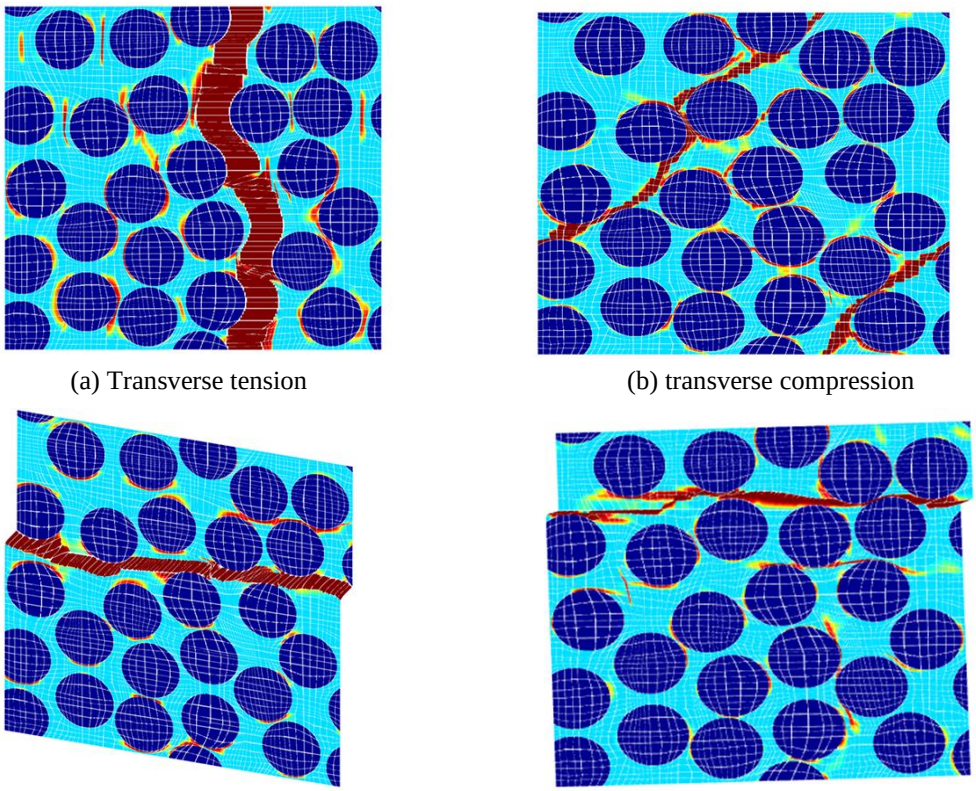

(a) Transverse tension (b) transverse compression

(c) longitudinal shear (d) transverse shear

Fig. 9 Field damage distribution with perfect-bonding assumption

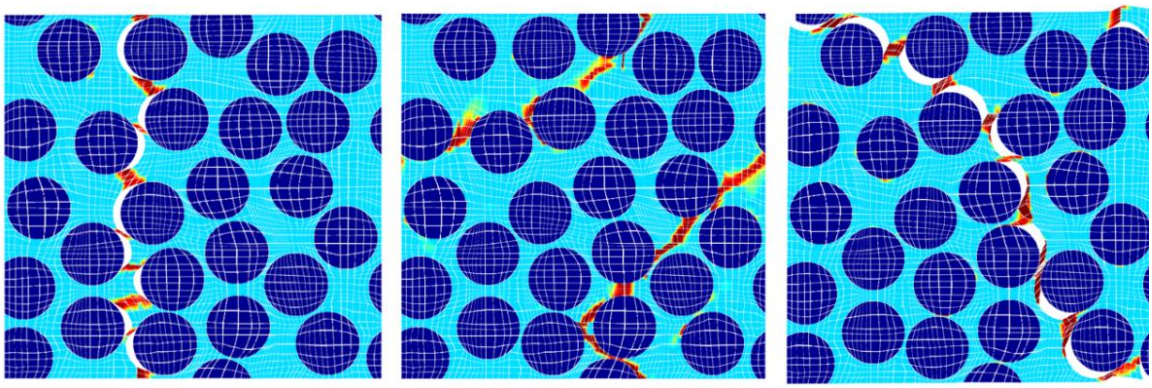

(a) Transverse tension (b) Transverse compression (c) Transverse shear

Fig. 10 Field damage distribution with cohesive zone modeling

damaged zones evolved among fibers. The aforementioned failure modes under shear loadings, represented in Figs. 9(c) and 10(c), are in excellent agreement with the damaged crack band reported by Melro *et al*. (2013).

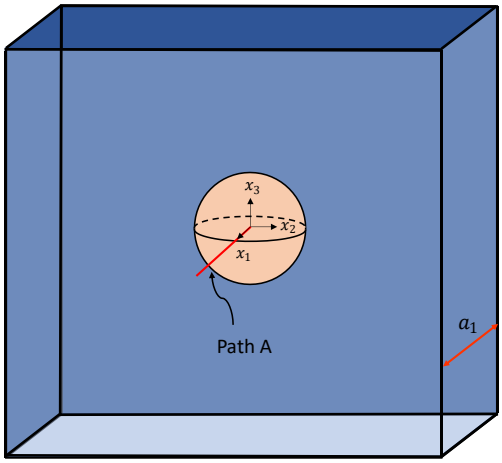

Fig. 11 Unit-cell with a central spherical micro-void

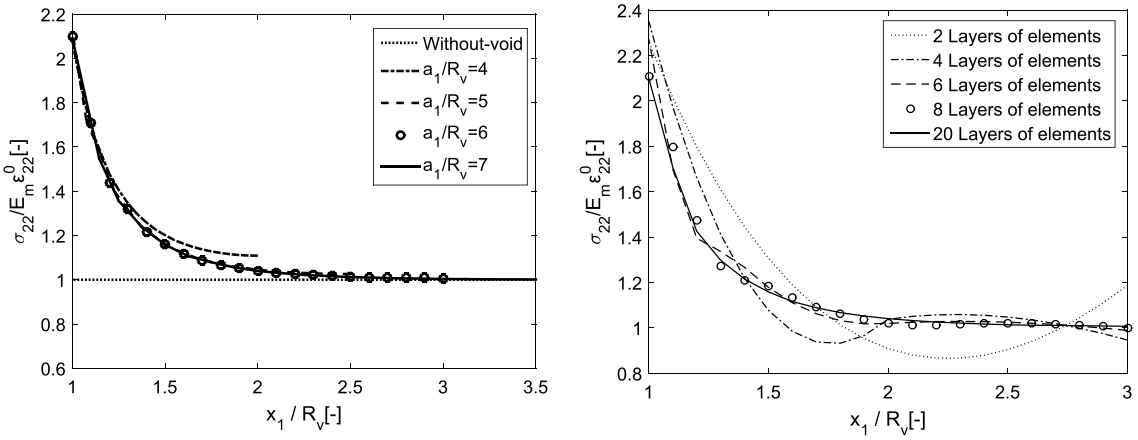

(a) With different thickness (b) With different number of layers along thickness

Fig. 12 Stress distribution on path-A

5.2 Example 2- Damage evaluation in UD-FRC, with micro-voids

Before the simulation of the RVE containing the micro-voids, a preliminary study was conducted on a unit-cell with a central spherical micro-void to define the appropriate thickness and number of required elements in the longitudinal direction. The schematic of the mentioned unit-cell is depicted in Fig. 11. In this research, micro-voids were assumed far from each other and the interaction among them was negligible (Mehdikhani, Petrov, *et al*. 2019b). So, the side edges of the periodic unit-cell were considered large enough, 10 times the void radius to satisfy the aforementioned condition. Similarly, the unit-cell thickness should be large enough to avoid the interaction effects of voids along the longitudinal direction. However, too large a thickness selection may increase the required layers of elements. Fig. 12(a) demonstrates that the stress

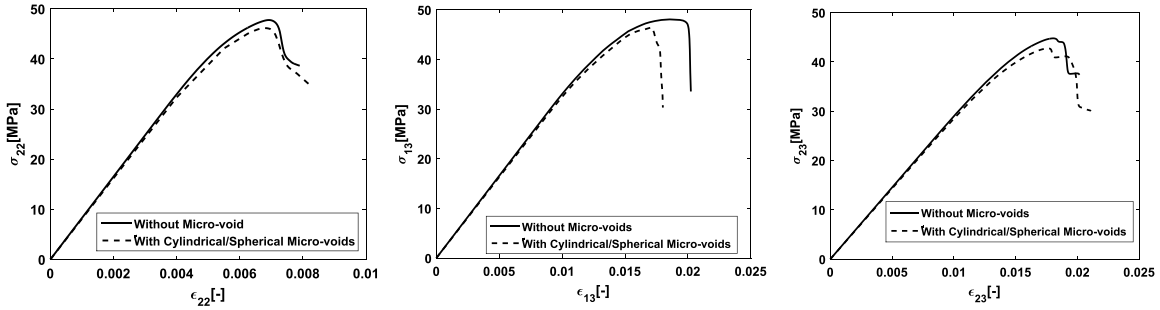

(a) Transverse tension (b) Transverse compression (c) Transverse shear

Fig. 13 Stress-Strain curves with and without micro-voids

Table 4 Obtained strengths with and without voids for different loading cases

Loading type	Strength [MPa] (Reduction percentage)	
	Without-void	With mixed cylindrical/spherical micro-voids
Transverse tension	47.8	46.2(3.6%)
Longitudinal shear	48.1	46.4(3.5%)

concentration dominated zone was about 2 times of the radius of spherical micro-void. Also, in cases with the $a_1/r_v \geq 5$, stress concentration was negligible near the external faces and almost equal to the nominal stress in a non-void unit-cell. As can be seen in Fig. 12(b), the results indicate that the stress field in IGA was converged by more than 6 layers of IGA elements. Based on this study, the RVE thickness was selected 6 times of the void radius. By using a few trial-and-errors, the optimum knot vector with 8 IGA elements along the fiber direction was selected as $Z = \{0,0,0,0.2,0.38,0.475,0.5,0.5,0.5,0.525,0.62,0.8,1,1,1\}$.

According to the displayed stress-strain curves in Fig. 13, at the beginning of loading to the RVE of Fig. 7(b), no significant change in the initial elastic stiffness was observed in the presence of micro-voids, which was justifiable due to the low volume fraction of voids. However, nonlinear behavior regions showed more compliance up to the final strength point. Since no plasticity was considered for the matrix, the nonlinear behavior region was only the consequence of damage evolution in the matrix and fiber/matrix interfaces. Therefore, increasing compliance in nonlinear regions indicates that micro-voids were promoting the activation of fracture mechanisms in composite. On the apex of stress-strain curves, reduction of strains on the peak loads were observed clearly. Especially, under longitudinal shear loading, there was a small horizontal region before reaching the peak load, which became shorter in the presence of micro-voids. Also, according to the obtained strengths in Table 4, most reduction of strength was reported to be ~5% for transverse shear loading.

Reasons for the aforementioned events were followed by studying damage evolution in void-containing RVEs. As can be seen in Fig. 14, damage distributions were plotted, which demonstrated that micro-voids could influence the final crack path in various types of loadings.

Under transverse tension, fracture initiation takes place by interface decohesion, without showing any considerable influence due to the presence of micro-voids. However, by increasing the tension load, initiated microcracks tended to some of the voids. The discussed failure mechanisms are in agreement with the results reported by Ashouri *et al*. (2014). As shown in Fig.

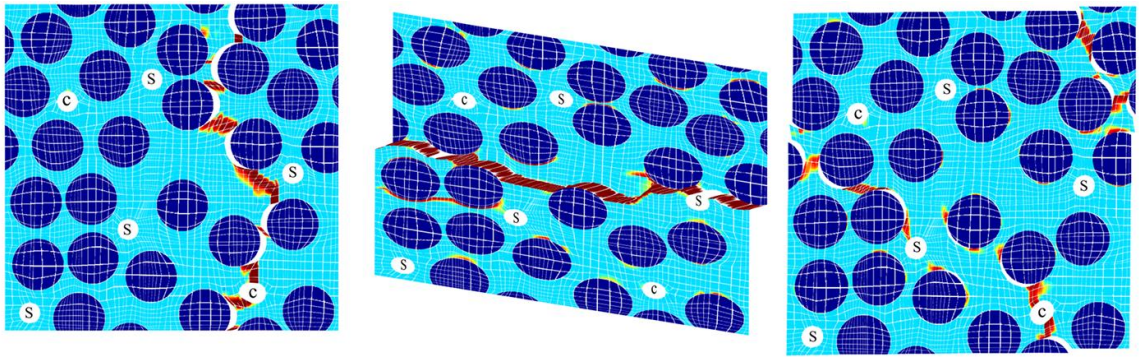

C: cylindrical micro-void S: spherical micro-void

(a) Transverse tension (b) Transverse compression (c) Transverse shear

Fig. 14 Contours of damage distribution in the presence of micro-voids

14(b), under longitudinal shear loading, microcracks initiated near the fiber/matrix interface before initiating near the micro-voids. However, As the applied load increased, microcracks near fibers tended to some of the micro-voids.

Under transverse shear loading, micro-voids played a more significant role and damage initiation occurred around the cylindrical micro-voids simultaneously with the interface decohesion. Eventually, the final crack band was formed with linking debonded interfaces, micro-cracks upon cylindrical micro-voids, and matrix cracking near debonded fibers.

6. Conclusions

A single-patch IGA-based framework was presented for micromechanical simulations of UD-FRD based on some step-by-step and easy-to-use techniques. The presented SPF was appropriate for the larger and more complicated RVEs, in contrast to MPA which required excess number of NURBS patches. This model was employed to generated RVEs subjected to different loading conditions. Comparing to FEM-based micromechanical damage analysis, the employed IGA-based method eliminates the geometrical approximation errors and simultaneously decreases the computational expenses, while retaining the accuracy. In this framework, some techniques were presented to model geometries with multiple voids in a single NURBS patch. By employing the offered techniques, the effects of presence of micro-voids on mechanical responses of UD-FRC were successfully simulated. Predicted damage evolutions and failure mechanisms were also in very good agreement with other experimental and numerical observations, thus confirming the veracity of the presented model in micromechanical damage analysis.

References

Alaydin, M.D., Behzadinasab, M. and Bazilevs, Y. (2022), "Isogeometric analysis of multilayer composite shell structures: Plasticity, damage, delamination and impact modeling", *Int. J. Solids Struct.*, **252**, 111782. https://doi.org/10.1016/j.ijsolstr.2022.111782.

Alberdi, R., Zhang, G. and Khandelwal, K. (2018), "A framework for implementation of RVE-based

multiscale models in computational homogenization using isogeometric analysis", *Int. J. Numer. Methods Eng.*, **114**(9), 1018-1051. https://doi.org/10.1002/nme.5775.

Arefi, A., van der Meer, F.P., Forouzan, M.R. and Silani, M. (2018), "Formulation of a consistent pressure-dependent damage model with fracture energy as input", *Compos. Struct.*, **201**, 208-216. https://doi.org/10.1016/j.compstruct.2018.06.005.

Arefi, A., van der Meer, F.P., Forouzan, M.R., Silani, M. and Salimi, M. (2020), "Micromechanical evaluation of failure models for unidirectional fiber-reinforced composites", *J. Compos. Mater.*, **54**(6), 791-800. https://doi.org/10.1177/0021998319867470.

Ashouri Vajari, D. (2015), "A micromechanical study of porous composites under longitudinal shear and transverse normal loading", *Compos. Struct.*, **125**, 266-276. https://doi.org/10.1016/j.compstruct.2015.02.026.

Ashouri Vajari, D., González, C., Llorca, J. and Legarth, B.N. (2014), "A numerical study of the influence of microvoids in the transverse mechanical response of unidirectional composites", *Compos. Sci. Technol.*, **97**, 46-54. https://doi.org/10.1016/j.compscitech.2014.04.004.

Barbero, E.J. (2008), *Finite Element Analysis of Composite Materials*, (First Edition), CRC press

Bazilevs, Y., Calo, V.M., Cottrell, J.A., Evans, J.A., Hughes, T.J.R., Lipton, S., Scott, M.A. and Sederberg, T.W. (2010), "Isogeometric analysis using T-splines", *Comput. Methods Appl. Mech. Eng.*, **199**(5-8), 229-263. https://doi.org/10.1016/j.cma.2009.02.036.

Bazilevs, Y., Deng, X., Korobenko, A., Lanza di Scalea, F., Todd, M.D. and Taylor, S.G. (2015), "Isogeometric fatigue damage prediction in large-scale composite structures driven by dynamic sensor data", *J. Appl. Mech.*, **82**(9) https://doi.org/10.1115/1.4030795.

Bhardwaj, G., Singh, I.V. and Mishra, B.K. (2015), "Fatigue crack growth in functionally graded material using homogenized XIGA", *Compos. Struct.*, **134**, 269-284. https://doi.org/10.1016/j.compstruct.2015.08.065.

Bhardwaj, G., Singh, S.K., Patil, R.U., Godara, R.K. and Khanna, K. (2021), "Thermo-elastic analysis of cracked functionally graded materials using XIGA", *Theor. Appl. Fract. Mech.*, **114**(May), 103016. https://doi.org/10.1016/j.tafmec.2021.103016.

Bhardwaj, G. and Singh, I.V. (2015), "Fatigue crack growth analysis of a homogeneous plate in the presence of multiple defects using extended isogeometric analysis", *J. Brazil. Soc. Mech. Sci. Eng.*, **37**(4), 1065-1082. https://doi.org/10.1007/s40430-014-0232-1.

Canal, L.P., González, C., Segurado, J. and LLorca, J. (2012), "Intraply fracture of fiber-reinforced composites: Microscopic mechanisms and modeling", *Compos. Sci. Technol.*, **72**(11), 1223-1232. https://doi.org/10.1016/j.compscitech.2012.04.008.

Chan, C.L., Anitescu, C. and Rabczuk, T. (2019), "Strong multipatch C1-coupling for isogeometric analysis on 2D and 3D domains", *Comput. Methods Appl. Mech. Eng.*, **357**, 112599. https://doi.org/10.1016/j.cma.2019.112599.

De Luycker, E., Benson, D.J., Belytschko, T., Bazilevs, Y. and Hsu, M.C. (2011), "X-FEM in isogeometric analysis for linear fracture mechanics", *Int. J. Numer. Methods Eng.*, **87**(6), 541-565. https://doi.org/10.1002/nme.3121.

Deng, X., Korobenko, A., Yan, J. and Bazilevs, Y. (2015), "Isogeometric analysis of continuum damage in rotation-free composite shells", *Comput. Methods Appl. Mech. Eng.*, **284**, 349-372. https://doi.org/10.1016/j.cma.2014.09.015.

Dimitri, R. and Zavarise, G. (2017), "Isogeometric treatment of frictional contact and mixed mode debonding problems", *Comput. Mech.*, **60**(2), 315-332. https://doi.org/10.1007/s00466-017-1410-7.

Dokken, T., Skytt, V., Haenisch, J. and Bengtsson, K. (2009), "Isogeometric Representation and Analysis: Bridging the Gap Between CAD and Analysis", *47th AIAA Aerosp. Sci. Meet. Incl. New Horizons Forum Aerosp. Expo.*, 1-10. https://doi.org/10.2514/6.2009-1172.

González, C. and LLorca, J. (2007), "Mechanical behavior of unidirectional fiber-reinforced polymers under transverse compression: Microscopic mechanisms and modeling", *Compos. Sci. Technol.*, **67**(13), 2795-2806. https://doi.org/10.1016/j.compscitech.2007.02.001.

Guo, Y., Do, H. and Ruess, M. (2019), "Isogeometric stability analysis of thin shells: From simple

geometries to engineering models", *Int. J. Numer. Methods Eng.*, **118**(8), 433-458. https://doi.org/10.1002/nme.6020.

Guo, Y., Ruess, M. and Schillinger, D. (2017), "A parameter-free variational coupling approach for trimmed isogeometric thin shells", *Comput. Mech.*, **59**(4), 693-715. https://doi.org/10.1007/s00466-016-1368-x.

Gurdal, Z., Tomasino, A.P. and Biggers, S.B. (1991), "effects of processing induced defects on laminate response - interlaminar tensile strength", *Sampe J.*, **27**

Hughes, T.J.R., Cottrell, J.A. and Bazilevs, Y. (2005), "Isogeometric analysis: CAD, finite elements, NURBS, exact geometry and mesh refinement", *Comput. Methods Appl. Mech. Eng.*, **194**(39), 4135-4195. https://doi.org/10.1016/j.cma.2004.10.008.

López, J., Anitescu, C. and Rabczuk, T. (2021), "Isogeometric structural shape optimization using automatic sensitivity analysis", *Appl. Math. Model.*, **89**, 1004-1024. https://doi.org/10.1016/j.apm.2020.07.027.

Matsubara, S., Nishi, S.-N. and Terada, K. (2017), "On the treatments of heterogeneities and periodic boundary conditions for isogeometric homogenization analysis", *Int. J. Numer. Methods Eng.*, **109**(11), 1523-1548. https://doi.org/10.1002/nme.5328.

Mehdikhani, M., Gorbatikh, L., Verpoest, I. and Lomov, S. V. (2019a), "Voids in fiber-reinforced polymer composites: A review on their formation, characteristics, and effects on mechanical performance", *J. Compos. Mater.*, **53**(12), 1579-1669. https://doi.org/10.1177/0021998318772152.

Mehdikhani, M., Petrov, N.A., Straumit, I., Melro, A.R., Lomov, S. V. and Gorbatikh, L. (2019b), "The effect of voids on matrix cracking in composite laminates as revealed by combined computations at the micro- and meso-scales", *Compos. Part A Appl. Sci. Manuf.*, **117**, 180-192. https://doi.org/10.1016/j.compositesa.2018.11.009.

Melro, A.R., Camanho, P.P. andrade Pires, F.M. and Pinho, S.T. (2013), "Micromechanical analysis of polymer composites reinforced by unidirectional fibres: Part II - Micromechanical analyses", *Int. J. Solids Struct.*, **50**(11-12), 1906-1915. https://doi.org/10.1016/j.ijsolstr.2013.02.007.

Naya, F., González, C., Lopes, C.S., Van der Veen, S. and Pons, F. (2017), "Computational micromechanics of the transverse and shear behavior of unidirectional fiber reinforced polymers including environmental effects", *Compos. Part A Appl. Sci. Manuf.*, **92**, 146-157. https://doi.org/10.1016/j.compositesa.2016.06.018.

Nguyen, V.P., Kerfriden, P. and Bordas, S.P.A. (2014), "Two- and three-dimensional isogeometric cohesive elements for composite delamination analysis", *Compos. Part B Eng.*, **60**, 193-212. https://doi.org/10.1016/j.compositesb.2013.12.018.

Pigazzini, M.S., Bazilevs, Y., Ellison, A. and Kim, H. (2018), "Isogeometric analysis for simulation of progressive damage in composite laminates", *J. Compos. Mater.*, **52**(25), 3471-3489. https://doi.org/10.1177/0021998318770723.

Puck, A. and Schürmann, H. (2002), "Failure analysis of FRP laminates by means of physically based phenomenological models", *Compos. Sci. Technol.*, **62**(12-13), 1633-1662. https://doi.org/10.1016/S0266-3538(01)00208-1.

Rawat, A., Piska, R., Rajagopal, A. and Hossain, M. (2021), "Nonlocal plasticity-based damage modeling in quasi-brittle materials using an isogeometric approach", *Eng. Comput.*, **38**(6), 2604-2630. https://doi.org/10.1108/EC-12-2019-0562.

Ruess, M., Schillinger, D., Özcan, A.I. and Rank, E. (2014), "Weak coupling for isogeometric analysis of non-matching and trimmed multi-patch geometries", *Comput. Methods Appl. Mech. Eng.*, **269**, 46-71. https://doi.org/10.1016/j.cma.2013.10.009.

Sederberg, T.W., Finnigan, G.T., Li, X., Lin, H. and Ipson, H. (2008), "Watertight trimmed NURBS", *ACM Trans. Graph.*, **27**(3), 1-8. https://doi.org/10.1145/1399504.1360678.

Shamloofard, M. and Assempour, A. (2019), "Development of an inverse isogeometric methodology and its application in sheet metal forming process", *Appl. Math. Model.*, **73**, 266-284. https://doi.org/10.1016/j.apm.2019.03.042.

Singh, I.V, Bhardwaj, G. and Mishra, B.K. (2015), "A new criterion for modeling multiple discontinuities passing through an element using XIGA", *J. Mech. Sci. Technol.*, **29**(3), 1131-1143. https://doi.org/10.1007/s12206-015-0225-8.

Terada, K., Hori, M., Kyoya, T. and Kikuchi, N. (2000), "Simulation of the multi-scale convergence in computational homogenization approaches", *Int. J. Solids Struct.*, **37**(16), 2285-2311. https://doi.org/10.1016/S0020-7683(98)00341-2.

Turon, A., Camanho, P.P., Costa, J. and Dávila, C.G. (2006), "A damage model for the simulation of delamination in advanced composites under variable-mode loading", *Mech. Mater.*, **38**(11), 1072-1089. https://doi.org/10.1016/j.mechmat.2005.10.003.

Verhoosel, C. V., Scott, M.A., de Borst, R. and Hughes, T.J.R. (2011a), "An isogeometric approach to cohesive zone modeling", *Int. J. Numer. Methods Eng.*, **87**(1-5), 336-360. https://doi.org/10.1002/nme.3061.

Verhoosel, C. V., Scott, M.A., Hughes, T.J.R. and de Borst, R. (2011b), "An isogeometric analysis approach to gradient damage models", *Int. J. Numer. Methods Eng.*, **86**(1), 115-134. https://doi.org/10.1002/nme.3150.

Willberg, C. (2016), "Analysis of the dynamical behavior of piezoceramic actuators using piezoelectric isogeometric finite elements", *Adv. Comput. Des.*, **1**(1), 37-60. https://doi.org/10.12989/acd.2016.1.1.037.

Yildizdag, M.E., Demirtas, M. and Ergin, A. (2020), "Multipatch discontinuous Galerkin isogeometric analysis of composite laminates", *Contin. Mech. Thermodyn.*, **32**(3), 607-620. https://doi.org/10.1007/s00161-018-0696-9.

CC